





Water coordinated on Cu(I)-based catalysts is the oxygen source in CO₂ reduction to CO

Yajun Zheng^{1,5}, Hedan Yao^{1,5}, Ruinan Di^{2,5}, Zhicheng Xiang¹, Qiang Wang ^{2✉}, Fangfang Lu¹, Yu Li¹, Guangxing Yang ^{3✉}, Qiang Ma ⁴ & Zhiping Zhang ^{1✉}

Catalytic reduction of CO₂ over Cu-based catalysts can produce various carbon-based products such as the critical intermediate CO, yet significant challenges remain in shedding light on the underlying mechanisms. Here, we develop a modified triple-stage quadrupole mass spectrometer to monitor the reduction of CO₂ to CO in the gas phase online. Our experimental observations reveal that the coordinated H₂O on Cu(I)-based catalysts promotes CO₂ adsorption and reduction to CO, and the resulting efficiencies are two orders of magnitude higher than those without H₂O. Isotope-labeling studies render compelling evidence that the O atom in produced CO originates from the coordinated H₂O on catalysts, rather than CO₂ itself. Combining experimental observations and computational calculations with density functional theory, we propose a detailed reaction mechanism of CO₂ reduction to CO over Cu(I)-based catalysts with coordinated H₂O. This study offers an effective method to reveal the vital roles of H₂O in promoting metal catalysts to CO₂ reduction.

¹School of Chemistry and Chemical Engineering, Xi'an Shiyou University, Xi'an 710065, China. ²School of Chemistry and Molecular Engineering, Nanjing Tech University, Nanjing 211816, China. ³School of Chemistry and Chemical Engineering, South China University of Technology, Guangzhou 510641, China. ⁴Chinese Academy of Inspection and Quarantine, Beijing 100176, China. ⁵These authors contributed equally: Yajun Zheng, Hedan Yao, Ruinan Di.
✉email: wangqiang@njtech.edu.cn; yanggx@scut.edu.cn; zhipingzhang@xsyu.edu.cn

Catalytic reduction of CO₂ into high value-added carbon-based products is a promising strategy for tackling current energy demands and reducing greenhouse gas emissions^{1–5}. In the past few years, tremendous efforts have been made to explore CO₂ reduction reaction (CO₂RR), and several products, including CH₄⁶, CO⁷, CH₃OH⁸, HCOOH⁹, HCHO¹⁰, C₂H₄¹¹, C₂H₆¹², C₂H₅OH¹³, and H₂C₂O₄¹⁴, have been generated from CO₂ reduction via photo-, electro-, or thermal activation^{3–5,15–18}. To enhance the selectivity and the conversion efficiency of CO₂RR, focus has primarily been on exploring novel catalysts^{2,3,19,20}. Despite the progress, many details of the CO₂RR mechanisms on the surface of catalysts remain elusive. The techniques used to investigate CO₂RR mechanisms include Raman spectroscopy²¹, X-ray absorption spectroscopy²², X-ray photoelectron spectroscopy²³, electron microscopy²⁴, and calculations using density functional theory (DFT)^{25,26}. However, direct observation of the highly reactive intermediates is still a grand challenge.

Mass spectrometry (MS) is a formidable tool for chemical analysis and has also been used to explore the mechanisms of various chemical reactions^{27–31}. Nevertheless, there have been few reports on the use of MS to study CO₂RR mechanisms in operando³². This could be attributed to the following obstacles: (i) CO₂ and its resulting products (e.g., CO, CH₄, and CH₃OH) are neutral molecules and rarely observed in mass spectra without adding charges through ionization; (ii) the lifetimes of reactive intermediates are typically less than milliseconds, making it challenging to capture them with off-line MS. To address these issues, this study proposes a strategy to explore CO₂RR mechanisms by adopting the features of triple-stage quadrupole (TSQ) mass spectrometer, in which different stages of quadrupoles in TSQ are used for separation of metal ions and related catalysts originating from nanoelectrospray ionization (nanoESI)³³ (first stage), reaction unit of metal catalysts and CO₂ (second stage), and transmission of resulting ions (third stage) (Fig. 1). In the second stage, CO₂ and its resulting products could be charged favorably by interacting with metal ions and forming metal complexes. More importantly, the CO₂RR processes can be simultaneously carried out with online detection. As such, the reaction pathways of CO₂RR can be well identified.

To demonstrate the proof-of-concept, this study explores the reduction reaction of CO₂ to CO using copper (Cu) as the catalyst. Cu is the only metal catalyst known to generate hydrocarbons through CO₂RR^{5,34–39}, but poor selectivity and reaction efficiency for value-added products significantly limit its commercial applications^{6,40}. Although much effort has been made to understand the catalytic performance of Cu in CO₂RR, available techniques that can clarify the underlying reaction mechanisms remain limited⁴¹. In the CO₂RR, CO has been widely identified as

a significant product or a primary reaction intermediate for the formation of hydrocarbons^{15–17,42,43}. Therefore, understanding the reduction reaction of CO₂ to CO over Cu-based catalysts is necessary to promote conversion efficiency.

According to general understanding, there are three routes in CO₂ reduction to CO: (i) CO₂ + H₂ → CO + H₂O^{1,17,44}, (ii) *CO₂ + 2e⁻ + H⁺ → CO + OH⁻⁴⁵, and (iii) *CO₂ + 2e⁻ + 2H⁺ → CO + H₂O^{43,46–50} (Fig. 1). For all three pathways, the O atom in the generated CO originated from CO₂. In contrast to the above routes, herein we discovered for the first time that the source of the O atom in CO originated from the H₂O coordinated on transition metal-based catalysts (e.g., Cu, Ag, and Pd) rather than CO₂. H₂O is ubiquitous in nature and has been shown to be vital in many reactions such as alcohol oxidation to aldehyde⁵¹, CH₄ oxidation to CH₃OH^{52,53}, and CO₂ reduction to CH₄, CH₃OH, and HCOOH⁵⁴. However, the role of H₂O in the reduction of CO₂ to CO is ambiguous. To elucidate the role of H₂O in CO₂RR, we investigated the behavior of Cu⁺ and [Cu(H₂O)]⁺ and found that the coordinated H₂O in [Cu(H₂O)]⁺ not only favored the adsorption of CO₂ onto Cu⁺, but also facilitated the reduction of CO₂ to CO. Isotope-labeling studies provided evidence suggesting that the origin of the O atom in CO was from the coordinated H₂O on Cu⁺. By combining experimental results and computational calculations with DFT, the detailed reaction mechanism of CO₂ reduction to CO over a [Cu(H₂O)]⁺ catalyst was proposed. The data presented in this work allowed us to elucidate the role of H₂O in CO₂RR and offered new insights for developing effective systems that enhanced the selectivity and conversion efficiency of CO₂ to CO and other carbon-based products.

Results and Discussion

Reaction apparatus and generation of Cu(I) species. To reveal the underlying roles of H₂O in the reduction of CO₂ to CO via copper-based catalysis, we employed a modified TSQ apparatus for online observation of the CO₂RR and detection of the reaction intermediates and products. As shown in Fig. 1, nanoESI was used as an ionization source to generate Cu-based ions. As the catalyst ions were introduced into the TSQ apparatus, the desired Cu species were isolated from Q1 and then transferred to Q2. In the reaction unit of Q2, Cu-based ions interacted with CO₂ upon the applied voltage of 5 V and formed CO. Due to the low reaction efficiency at low temperatures (as discussed below), CO₂ gas was heated to 280 °C using a heating tape in the gas circuit system prior to reacting with the Cu catalyst in the gas phase. After the reduction reaction was completed, the resulting products were transferred directly to Q3 followed by online detection.

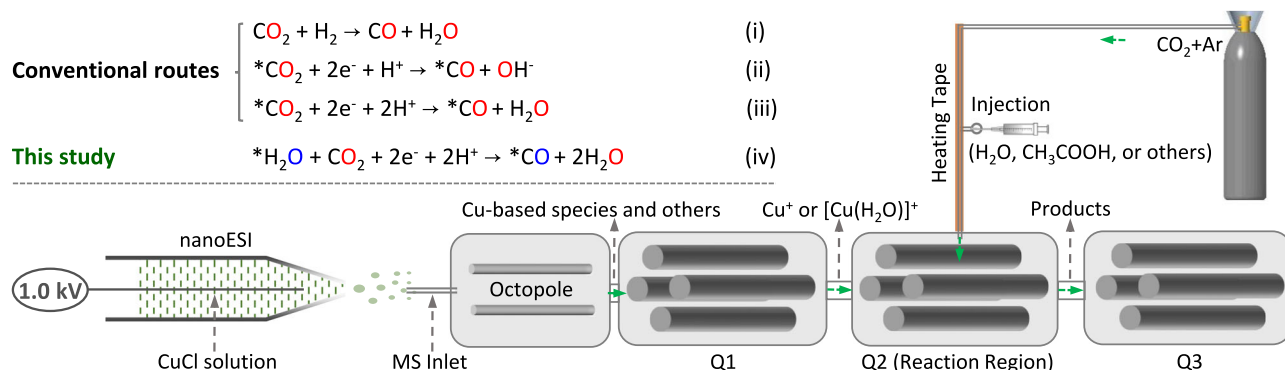


Fig. 1 Schematic diagram of the apparatus for CO₂ reduction and detection of reaction products. (insets in the top left corner are the different routes for generation of CO from CO₂, in which * means catalyst).

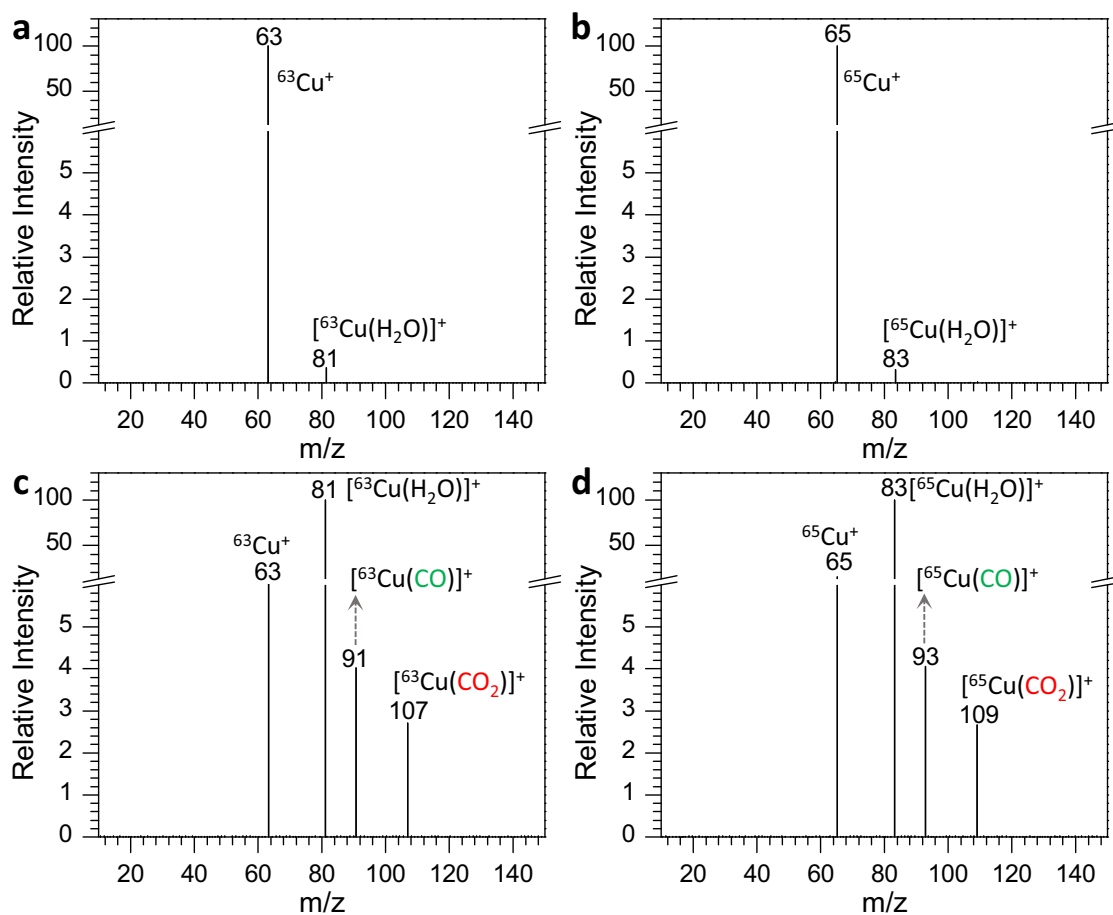


Fig. 2 Mass spectra of CO₂ reduction to CO under different Cu-based catalytic systems. **a** ⁶³Cu⁺ **b** ⁶⁵Cu⁺. **c** [⁶³Cu(H₂O)]⁺. **d** [⁶⁵Cu(H₂O)]⁺ (gas circuit temperature: 280 °C; reaction pressure: 1.5 mTorr).

Many previous studies^{8,26,55–59} have demonstrated that of the different oxidation states, Cu(I)-related species are one of the most important catalysts in CO₂RR. Considering that the current study investigated different Cu-based complexes in the reduction of CO₂, nanoESI was utilized to generate Cu(I) species rather than inductively coupled plasma (ICP)^{60,61}, which only produces Cu(I). In the nanoESI process, the types of Cu species and solvent were found to have a pronounced effect on the resulting mass spectra. When CuX (X = Cl, Br, or I) was dissolved into acetonitrile, comparable and intensive peaks of Cu-based ions appeared in the mass spectra (e.g., ⁶³Cu⁺, ⁶⁵Cu⁺, [⁶³Cu(H₂O)]⁺, and [⁶⁵Cu(H₂O)]⁺), and few non-Cu species emerged (Supplementary Figs. 1–3). Thus, CuCl was used to generate different Cu(I)-based ions.

Effect of H₂O on the reduction of CO₂ to CO. The above MS setup allowed us to investigate the reduction of CO₂ to CO in situ. As ⁶³Cu⁺ or ⁶⁵Cu⁺ ions were isolated to interact with CO₂, no obvious resultant species were observed, and only Cu⁺ itself and [Cu(H₂O)]⁺ appeared in the mass spectra (Fig. 2a, b). Remarkably, when [⁶³Cu(H₂O)]⁺ or [⁶⁵Cu(H₂O)]⁺ was introduced to the reaction unit along with CO₂, not only did the reaction product, CO, emerge in the forms of [⁶³Cu(CO)]⁺ and [⁶⁵Cu(CO)]⁺, but so did the reactant, CO₂, as complexes of [⁶³Cu(CO₂)]⁺ and [⁶⁵Cu(CO₂)]⁺, in addition to [⁶³Cu(H₂O)]⁺, [⁶⁵Cu(H₂O)]⁺, and their fragment ions ⁶³Cu⁺ and ⁶⁵Cu⁺ (Fig. 2c, d). These results suggested that in contrast to the bare Cu⁺, the coordinated H₂O in [Cu(H₂O)]⁺ played a vital role in the interaction with CO₂, which both rendered the adsorption of

CO₂ and the reduction of CO₂ to CO on the Cu(I) catalyst. We also found that the coordinated H₂O favored other metal-based ions (e.g., [Ag(H₂O)]⁺ and [Pd(H₂O)]⁺) to carry out the CO₂RR (Supplementary Figs. 4 and 5), revealing that H₂O molecules on the metal catalysts were active sites for facilitating the effective reduction of CO₂ to CO. The effect of H₂O could also be mirrored by a reversed water-gas shift reaction (WGSR) using Cu/ZnO/Al₂O₃ as catalyst (Supplementary Fig. 6a–c) and in situ diffuse reflectance infrared Fourier transform spectroscopy (in situ DRIFTS) using Cu/γ-Al₂O₃ and Pt/γ-Al₂O₃ as catalysts (Supplementary Fig. 7). It hinted that dosing a suitable amount of H₂O could promote heterogeneous thermal catalytic conversion of CO₂ to CO in realistic conditions.

To quantitatively describe the roles of coordinated H₂O over metal surfaces to CO₂ adsorption and reduction to CO, we used Cu-based catalysts as an example. Fig. 3a and Supplementary Fig. 8a show the effect of reaction gas pressure on the adsorption of CO₂ to Cu⁺. The adsorption performance was examined by the absolute peak intensities of generated [Cu(CO₂)]⁺ in mass spectrometric analysis. When bare Cu⁺ was employed, the adsorption ability of CO₂ onto the Cu⁺ catalyst gradually increased with the increasing reaction gas pressure from 0 to 4 mTorr. However, in the presence of [Cu(H₂O)]⁺, the adsorption of CO₂ onto Cu⁺ increased with increasing reaction gas pressure and reached a maximum value in the range of 1.5 – 2.5 mTorr, then decreased thereafter. More interestingly, in the presence of [⁶³Cu(H₂O)]⁺, the peak intensity of [⁶³Cu(CO₂)]⁺ was 48.6-fold higher than that with ⁶³Cu⁺ in their optimal conditions. This demonstrated that after H₂O was coordinated to

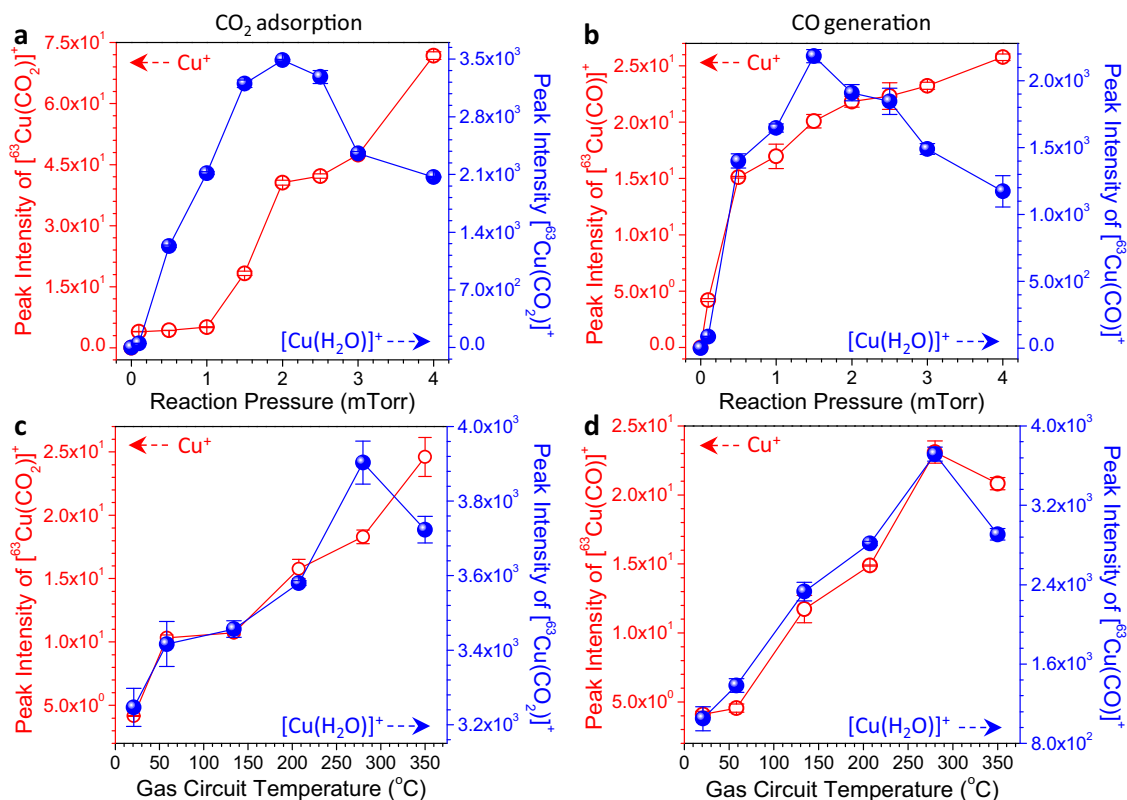


Fig. 3 Variation of CO₂ adsorption and CO generation with reaction pressure and temperature of heating tape around the gas circuit. Effect of reaction pressure on (a) the adsorption of CO₂ onto ⁶³Cu⁺ and (b) CO generation by CO₂ reduction in the presence of either ⁶³Cu⁺ or [⁶³Cu(H₂O)]⁺ catalysts (gas circuit temperature: 280 °C). Effect of the gas circuit temperature on (c) the adsorption of CO₂ onto Cu⁺ and (d) CO generation by CO₂ reduction in the presence of either ⁶³Cu⁺ or [⁶³Cu(H₂O)]⁺ catalysts (reaction pressure: 1.5 mTorr).

Cu⁺, CO₂ was more prone to interact with [⁶³Cu(H₂O)]⁺ to generate [⁶³Cu(CO₂)]⁺ compared to bare Cu⁺. Besides CO₂, we also found that in contrast to Cu⁺, [Cu(H₂O)]⁺ was likely to form Cu-based complexes with other molecules such as methanol (Supplementary Fig. 9), ethanol (Supplementary Fig. 10), acetonitrile (Supplementary Fig. 11), benzene (Supplementary Fig. 12), toluene (Supplementary Fig. 13), and dichloromethane (Supplementary Fig. 14). Such a fact suggests that the coordinated H₂O in the structure of [Cu(H₂O)]⁺ is a uniquely active site for adsorbing different molecules. To our knowledge, it could be speculated as the following reasons. As H₂O was bound to Cu⁺, the resulting [Cu(H₂O)]⁺ more likely tended to form hydrogen bond^{62–66} or OH-π interactions^{67–69} with those studied molecules than bare Cu⁺. After undergoing further structural rearrangements, Cu(I)-based complexes were favorably generated. Despite this, detailed reasons need to be further studied.

It is well known that adsorption onto catalyst surfaces is a very crucial step for CO₂ reduction, and a more favorable CO₂ adsorption can facilitate a more efficient reduction to CO¹⁵. To evaluate the reduction ability of CO₂ to CO in the presence of Cu⁺ and [Cu(H₂O)]⁺, we compared the difference in quantity of generated [Cu(CO)]⁺ at varying gas pressures (Fig. 3b and Supplementary Fig. 8b). For bare Cu⁺, the peak intensity of [⁶³Cu(CO)]⁺ sharply increased at 0 – 0.5 mTorr, followed by a gradual increase at 1 – 4 mTorr. A different pattern was observed for [Cu(H₂O)]⁺, where the peak intensity first increased to a maximum value at 1.5 mTorr, and then decreased thereafter. Comparing both systems with Cu⁺ and [Cu(H₂O)]⁺, it was remarkable that [Cu(CO)]⁺ was generated more favorably for [Cu(H₂O)]⁺. Similar to the amount of adsorbed CO₂, the amount of CO generated in the presence of [⁶³Cu(H₂O)]⁺ was 84.7-fold

higher than that in the presence of ⁶³Cu⁺ under optimal conditions. These results indicated that the coordinated H₂O in [⁶³Cu(H₂O)]⁺ not only greatly facilitated CO₂ adsorption to Cu⁺, but also significantly promoted CO generation.

A similar process was also conducted to compare the adsorption of CO₂ and generation of CO at different temperatures, which was controlled by varying the temperature of heating tape around the gas circuit (Fig. 1). As the temperature increased from room temperature (20 °C) to 350 °C, CO₂ adsorption using ⁶³Cu⁺ demonstrated a gradual increasing pattern. However, a different pattern was observed for the system using [⁶³Cu(H₂O)]⁺, in which an initial steady increasing trend from room temperature to 280 °C was observed, followed by a slight decreasing one within the range of 280 – 350 °C (Fig. 3c and Supplementary Fig. 8c). In the optimal temperature range, the CO₂ adsorption amount in the presence of [⁶³Cu(H₂O)]⁺ was more than two orders of magnitude (158.7-fold) higher than ⁶³Cu⁺. For the generation of CO, both ⁶³Cu⁺ and [⁶³Cu(H₂O)]⁺ catalytic systems demonstrated a comparable pattern, in which the formation of CO first increased and reached a maximum value at 280 °C, then decreased thereafter (Fig. 3d and Supplementary Fig. 8d). By comparing both systems, it was found that the use of [⁶³Cu(H₂O)]⁺ resulted in more than two orders of magnitude (160.9-fold) of CO formation than using ⁶³Cu⁺. Thus, we can conclude in confident that the coordinated H₂O in [⁶³Cu(H₂O)]⁺ was a governing factor in CO₂ adsorption and CO generation.

From the above, it was noticeable that there was a maximum CO₂ adsorption capacity and a maximum CO production rate when [Cu(H₂O)]⁺ was used as catalyst throughout the studied temperature and pressure ranges (Fig. 3). This phenomenon was presumably due to the instability of [Cu(H₂O)]⁺ with increasing

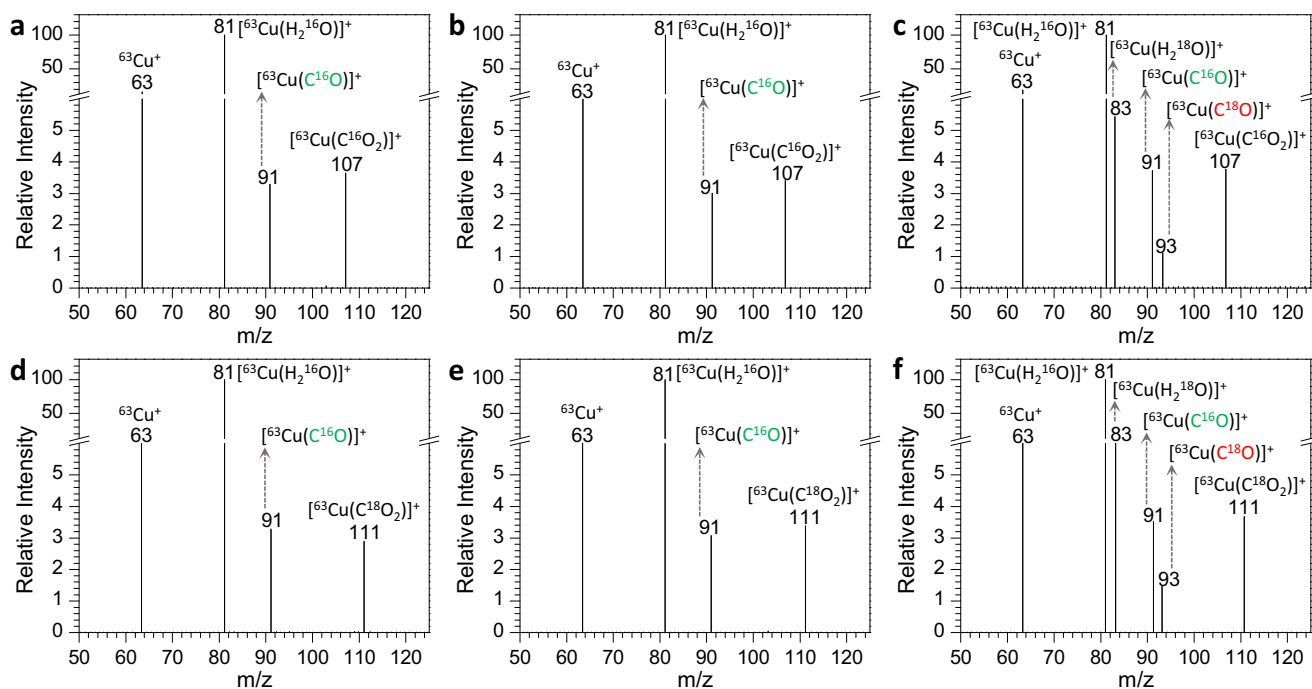


Fig. 4 Isotope-labeling MS measurement results under different systems. **a** $[^{63}\text{Cu}(\text{H}_2^{16}\text{O})]^+$ and C^{16}O_2 . **b** $[^{63}\text{Cu}(\text{H}_2^{16}\text{O})]^+$, H_2^{16}O , and C^{16}O_2 . **c** $[^{63}\text{Cu}(\text{H}_2^{16}\text{O})]^+$, H_2^{18}O , and C^{16}O_2 . **d** $[^{63}\text{Cu}(\text{H}_2^{16}\text{O})]^+$ and C^{18}O_2 . **e** $[^{63}\text{Cu}(\text{H}_2^{16}\text{O})]^+$, H_2^{16}O , and C^{18}O_2 . **f** $[^{63}\text{Cu}(\text{H}_2^{16}\text{O})]^+$, H_2^{18}O and C^{18}O_2 (gas circuit temperature: 280 °C; reaction pressure: 1.5 mTorr).

reaction pressures and temperatures. As an example of increasing reaction pressures, the content of CO_2 in the Q2 of mass spectrometer (Fig. 1) steadily increased and therefore, high yields of $[\text{Cu}(\text{CO}_2)]^+$ and $[\text{Cu}(\text{CO})]^+$ should be generated, whereas an opposite trend was observed within the range of 2 – 4 mTorr (Fig. 3a, b). As aforementioned, $[\text{Cu}(\text{H}_2\text{O})]^+$ was more favorable for the generation of $[\text{Cu}(\text{CO}_2)]^+$ and $[\text{Cu}(\text{CO})]^+$ than Cu^+ . However, the generated amount of $[\text{Cu}(\text{H}_2\text{O})]^+$ demonstrated a decreasing pattern with increasing reaction pressures from 2 to 4 mTorr (Supplementary Fig. 15a). A lower amount of $[\text{Cu}(\text{H}_2\text{O})]^+$ would result in a lower generation efficiency to $[\text{Cu}(\text{CO}_2)]^+$ and $[\text{Cu}(\text{CO})]^+$. As a compromise between reaction pressure and the amount of $[\text{Cu}(\text{H}_2\text{O})]^+$, 1.5 mTorr gave the optimal performance. As to the temperature, the same pattern as the reaction pressure was observed (Fig. 3c, d), and 280 °C offered the highest generation efficiencies to both $[\text{Cu}(\text{CO}_2)]^+$ and $[\text{Cu}(\text{CO})]^+$. This case may be associated with the compromise of $[\text{Cu}(\text{H}_2\text{O})]^+$ stability (Supplementary Fig. 15b) and the thermodynamic reaction activity between CO_2 and $[\text{Cu}(\text{H}_2\text{O})]^+$ under increasing temperatures.

Origin of the O atom in generated CO. Isotope-labeling experiments (H_2^{16}O , H_2^{18}O , C^{16}O_2 , and C^{18}O_2) allowed us to conclude that the origin of the O atom in the generated CO was from the coordinated H_2O , rather than CO_2 itself. In previous studies^{1,17,34,43–50}, different mechanistic scenarios were proposed to elucidate the reduction pathway of CO_2 to CO, and the generation of CO was conventionally contributed to the loss of an O atom in CO_2 . However, no direct experimental evidence generated through isotopic labeling has been supported thus so far. MS has been demonstrated to be a very powerful tool that offers the opportunity to derive the origin of the O atom in generated CO from CO_2 .

As expected, monitoring of the reaction between $[^{63}\text{Cu}(\text{H}_2^{16}\text{O})]^+$ and C^{16}O_2 resulted in the observation of $[^{63}\text{Cu}(\text{C}^{16}\text{O})]^+$ (Fig. 4a). The inability to isolate $[^{63}\text{Cu}(\text{H}_2^{18}\text{O})]^+$, by dissolving CuCl or other Cu-based chemicals into the mixture of acetonitrile and H_2^{18}O ,

meant that it was impossible to probe the reaction products in the presence of $[^{63}\text{Cu}(\text{H}_2^{18}\text{O})]^+$ and C^{16}O_2 . This case could be attributable to the fact that there are plenty of H_2^{16}O in air, and the H_2^{18}O in generated $[^{63}\text{Cu}(\text{H}_2^{18}\text{O})]^+$ would be quickly exchanged by H_2^{16}O in the plume of nanoESI or the transfer process to the Q1 of mass spectrometer (Fig. 1). As a result, insufficient $[^{63}\text{Cu}(\text{H}_2^{18}\text{O})]^+$ ions could be generated and were not favorable for MS detection. To resolve this issue, $[^{63}\text{Cu}(\text{H}_2^{16}\text{O})]^+$ was first isolated in Q1, and H_2^{16}O or H_2^{18}O was then injected into the CO_2 gas circuit (Fig. 1). After interaction among the reactants in the reaction region Q2, the resulting products were analyzed. As H_2^{16}O was injected (Fig. 4b), the mass spectrum was analogous to that of only $[^{63}\text{Cu}(\text{H}_2^{16}\text{O})]^+$ and C^{16}O_2 (Fig. 4a). Noticeably, when H_2^{18}O was added to the system containing $[^{63}\text{Cu}(\text{H}_2^{16}\text{O})]^+$ and C^{16}O_2 (Fig. 4c), not only did $[^{63}\text{Cu}(\text{H}_2^{18}\text{O})]^+$ appear in the mass spectrum, but so did $[^{63}\text{Cu}(\text{C}^{16}\text{O})]^+$ and $[^{63}\text{Cu}(\text{C}^{18}\text{O})]^+$. These results indicated that it was an effective strategy for generating $[^{63}\text{Cu}(\text{H}_2^{18}\text{O})]^+$, and more importantly, the origin of the O atom in CO was presumable from the coordinated water.

More convincing evidence was gained from the reaction between $[^{63}\text{Cu}(\text{H}_2^{16}\text{O})]^+$, C^{18}O_2 , and $\text{H}_2^{16}\text{O}/\text{H}_2^{18}\text{O}$. Interestingly, as $[^{63}\text{Cu}(\text{H}_2^{16}\text{O})]^+$ interacted with C^{18}O_2 (Fig. 4d), $[^{63}\text{Cu}(\text{C}^{16}\text{O})]^+$, rather than $[^{63}\text{Cu}(\text{C}^{18}\text{O})]^+$, was formed, indicating that the O atom in CO was indeed from the H_2O . The same result was obtained from the system with $[^{63}\text{Cu}(\text{H}_2^{16}\text{O})]^+$, C^{18}O_2 , and H_2^{16}O (Fig. 4e). However, as H_2^{18}O was injected into the C^{18}O_2 gas circuit system (Fig. 4f), the mass spectrum was analogous to the system with $[^{63}\text{Cu}(\text{H}_2^{16}\text{O})]^+$, C^{16}O_2 and H_2^{18}O (Fig. 4c), in which both $[^{63}\text{Cu}(\text{C}^{16}\text{O})]^+$ and $[^{63}\text{Cu}(\text{C}^{18}\text{O})]^+$ were generated. This phenomenon, as well as ^{65}Cu (Supplementary Fig. 16), ^{107}Ag , and ^{104}Pd (Supplementary Fig. 17)-based reactions, allowed us to draw a definite conclusion that in the CO_2RR process, the two O atoms in CO_2 were eliminated completely by losses of two molecules of H_2O ^{46,48,70}, and the O atom in CO originated from the coordinated H_2O . Moreover, H_2^{18}O -labeling experiments in tandem with off-line GC-MS

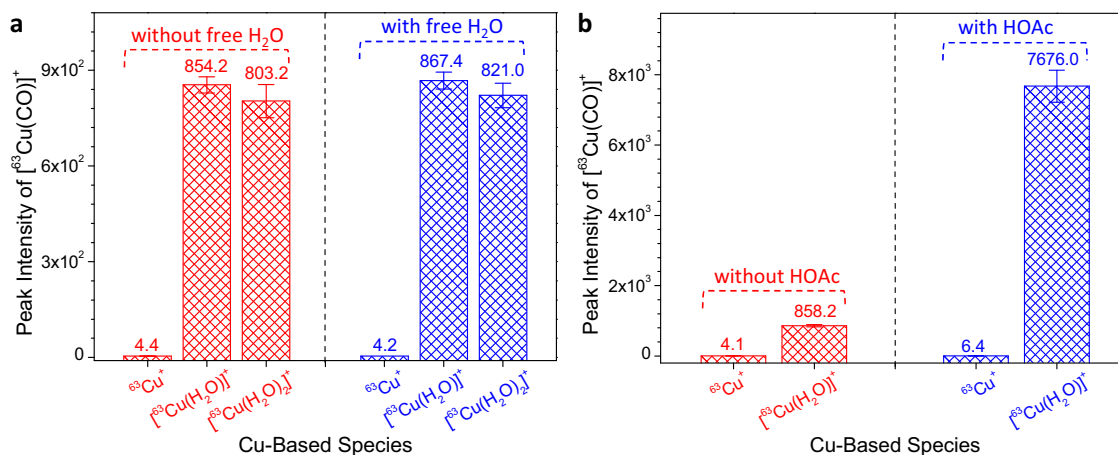


Fig. 5 Influence of the number of coordinated H₂O, free H₂O, and extraneous acid on the generation of CO. **a** Effects of the number of coordinated H₂O and free H₂O on CO₂ reduction to CO under different Cu-based catalytic systems ($^{63}\text{Cu}^+$, $[^{63}\text{Cu}(\text{H}_2\text{O})]^+$, and $[^{63}\text{Cu}(\text{H}_2\text{O})_2]^+$). **b** Effect of extraneous acid on the reduction of CO₂ to CO under different Cu-based catalytic systems. Note: The free H₂O and HOAc (acetic acid) were injected into the gas circuit system by an injector; gas circuit temperature: 280 °C; reaction pressure: 1.5 mTorr; $n = 5$).

analysis were carried out to confirm the source of O atom in resulting CO from the reversed WGS. As shown in Supplementary Fig. 6f–h, in comparison with the system of introducing H₂¹⁶O, an abundant peak of m/z 30 (C¹⁸O) emerged in the mass spectrum for the system of H₂¹⁸O. This fact indicated that the involved H₂O was the oxygen source of the resulting CO. More importantly, the observed results of CO₂ reduction in the TSQ mass spectrometer could be extrapolated to realistic heterogeneous catalysis. Those gas-phase results also correlated directly to solution-phase CO₂RR. To gain insight into this point, we performed the electrochemical reduction of CO₂ in KCl aqueous solution using Au electrode, because the produced amount of CO was below the limit of detection using Cu or Ag electrode. The reaction products were monitored using an online differential electrochemical mass spectrometer (Supplementary Fig. 18). In contrast to the system of H₂¹⁶O, a considerable amount of C¹⁸O (m/z 30) was generated in the presence of H₂¹⁸O (Supplementary Figs. 19–21). This further indicated that H₂O was the oxygen source of resulting CO from CO₂ reduction and provided solid evidence on the generalization of the current finding to related reactions in the condensed phase (Supplementary Table 1).

Identifying the effect of H₂O on CO generation. The number of coordinated H₂O in $[^{63}\text{Cu}(\text{H}_2\text{O})_x]^+$ ($x = 0, 1, \text{ or } 2$) was observed to have a significant influence on the reduction of CO₂ to CO. The reaction efficiency was evaluated by comparing the absolute peak intensities of generated $[^{63}\text{Cu}(\text{CO})]^+$ in mass spectrometric analysis. When bare $^{63}\text{Cu}^+$ was used as the catalyst, a low signal was observed (Fig. 5a and Supplementary Fig. 22). Noticeably, a significant improvement was observed for $[^{63}\text{Cu}(\text{H}_2\text{O})]^+$, and the reaction efficiency was 193.8 times higher than with $^{63}\text{Cu}^+$. However, further increasing the number of coordinated H₂O to 2 (e.g., $[^{63}\text{Cu}(\text{H}_2\text{O})_2]^+$) resulted in a comparable reaction efficiency to $[^{63}\text{Cu}(\text{H}_2\text{O})]^+$, indicating that one coordinated H₂O molecule was sufficient for high-efficiency reduction of CO₂ to CO.

In the reaction between $[^{63}\text{Cu}(\text{H}_2\text{O})]^+$ and CO₂, it was unclear how H₂O molecules interacted with CO₂, namely whether it was a (i) direct interaction between $[^{63}\text{Cu}(\text{H}_2\text{O})]^+$ and CO₂, or if (ii) CO₂ first interacted with the dissociated H₂O molecule from $[^{63}\text{Cu}(\text{H}_2\text{O})]^+$, then reacted with dissociated $^{63}\text{Cu}^+$ or $[^{63}\text{Cu}(\text{H}_2\text{O})]^+$. To probe the above assumptions, 2 μL of free H₂O was injected into the CO₂ gas circuit system at a temperature of 280 °C (Fig. 1). After being injected, the free H₂O molecules

immediately evaporated and interacted with CO₂ in the gas circuit by forming H₂CO₃ ($\text{H}_2\text{O} + \text{CO}_2 \rightarrow \text{H}_2\text{CO}_3$)^{71–73}, which was indirectly confirmed by the isotope-labeling experiments, namely H₂¹⁸O and C¹⁶O₂ (Supplementary Fig. 23). If route (ii) was taken in the CO₂RR, the involved free H₂O would facilitate CO₂ reduction to CO. However, a comparable reaction efficiency to the system without free H₂O was observed (Fig. 5a and Supplementary Fig. 22), indicating that CO₂ reduction to CO occurred through route (i). Namely, $[\text{Cu}(\text{H}_2\text{O})]^+$ first interacted with CO₂ by a formation of $[\text{Cu}(\text{H}_2\text{O})(\text{CO}_2)]^+$, which was supported by isotope-labeling experiments (Supplementary Fig. 24), and then a reduction reaction occurred to convert CO₂ to CO. The above results also indicated that the coordinated H₂O on the Cu⁺, rather than free H₂O, played crucial roles for the reduction of CO₂ to CO. The transition metals such as Cu⁺ not only provided efficient active sites for the generation of $[\text{Cu}(\text{H}_2\text{O})]^+$ or other H₂O-based metal complex ions, but also offered opportunity to charge neutral species such as CO₂ and CO for favorable mass spectrometric analysis by the forms of $[\text{Cu}(\text{CO}_2)]^+$ and $[\text{Cu}(\text{CO})]^+$ (Figs. 2 and 4).

Based on the prior experiments, the origin of the O atom in CO was from H₂O rather than CO₂. Thus, the two O atoms in CO₂ needed to be eliminated prior to the formation of CO. According to the previous CO₂RR mechanisms^{46,48,70}, the generation of CO was achieved by first proton-electron (H^+/e^-) transfer processes to CO₂, followed by the elimination of H₂O. To promote the formation of CO, an efficient step to proton generation and capture was necessary⁴⁶. In this study, a proton (H^+) was also found to be crucial to the generation of CO. For the reaction of $[\text{Cu}(\text{H}_2\text{O})]^+$ and CO₂, the generation of H^+ was believed to be caused by water dissociation. However, further dissociation of water might affect its ability to participate in the formation of $[\text{Cu}(\text{H}_2\text{O})(\text{CO}_2)]^+$ and reduce the reaction efficiency. Addition of supplementary H^+ could mitigate water dissociation and boost CO generation. To confirm this hypothesis, 2 μL of acetic acid (HOAc) was injected into the CO₂ gas circuit system. For the system containing $[\text{Cu}(\text{H}_2\text{O})]^+$, a 8.9-fold increase of CO formation was observed with the addition of HOAc, whereas no significant difference was observed for bare Cu⁺ (Fig. 5b and Supplementary Figs. 25 and 26). These results indicated that supplementary H^+ was indeed important for boosting the reduction efficiency of CO₂ to CO in the presence of $[\text{Cu}(\text{H}_2\text{O})]^+$ catalyst, in which H^+ from the coordinated H₂O participated into the elimination of O atoms in CO₂^{46,48,70}.

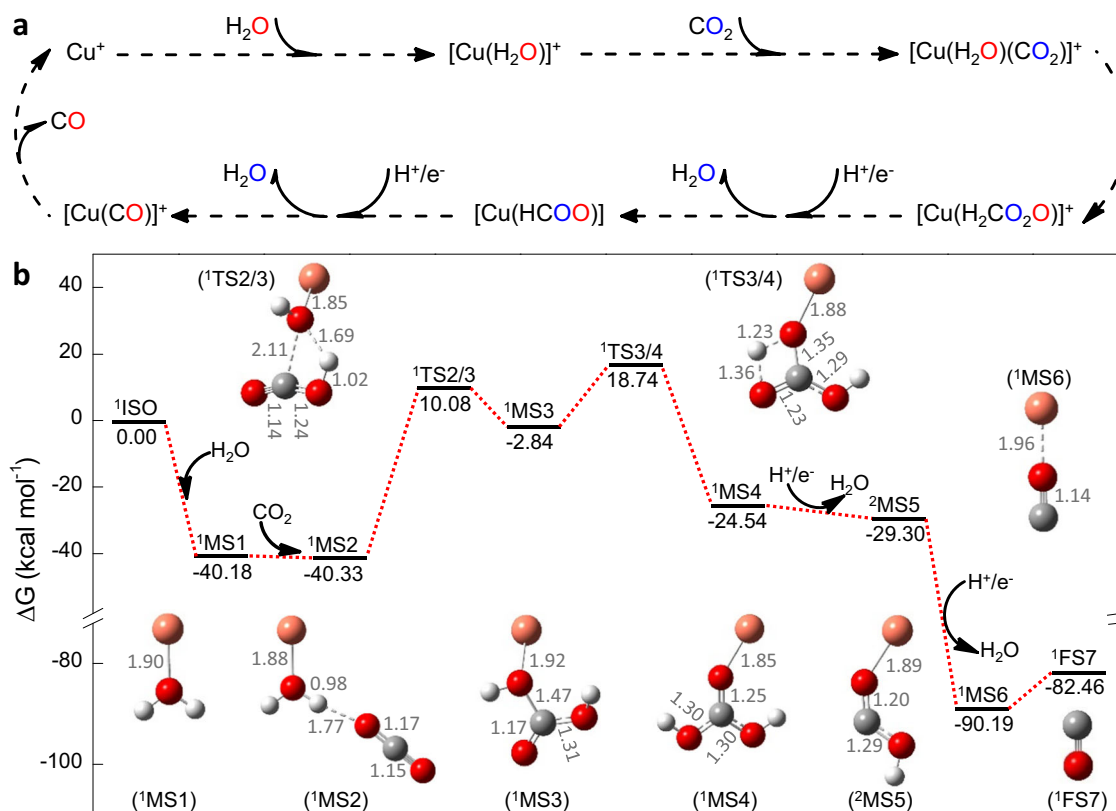


Fig. 6 The mechanism of CO₂ reduction to CO in the presence of Cu(I) catalyst and water. **a** Schematic representation of the reduction of CO₂ to CO according to experimental observations. **b** The DFT microscopic reaction pathway [the singlet reactants of ¹Cu⁺ + ¹H₂O + ¹CO₂ (¹ISO, 0.00) was taken to be zero as a reference], demonstrating the thermodynamic and kinetic feasibility of the suggested pathway.

Many previous studies^{8,26,55–59,74,75} illustrated that the Cu(I) surface was the active site anchoring the CO₂RR. Because of this, several strategies, including the addition of oxygen⁵⁹ or copper nitride support⁷⁶, boron-element doping³⁹, plasma treatment⁷⁷, catalyst electro-redeposition⁷⁸, and covering the catalyst surface with nanocavities⁵⁵, have been used to stabilize the active Cu(I) oxidation state. Despite these efforts, the precise effect of a single Cu valence state on the reduction of CO₂ to CO remains ambiguous. Ions can be easily isolated through MS, enabling the investigation of the interaction between CO₂ and Cu with different oxidation states. In this study, we not only investigated the effect of Cu(I) in CO₂RR, but also explored the performance of Cu(II) on CO production. Taking the copper oxidation state and the aforementioned H₂O effect into account, [⁶³Cu(OH)·H₂O]⁺ and [⁶⁵Cu(OH)·H₂O]⁺ (Supplementary Fig. 27a, b) were isolated to interact with CO₂. However, in contrast to the Cu(I) system (Fig. 4), a much lower amount of [⁶³Cu(CO)]⁺ or [⁶⁵Cu(CO)]⁺ was observed in the mass spectrum (Supplementary Fig. 27c, d). These results indicated that Cu(I) was better at reducing CO₂ to CO than Cu(II) even in the presence of water, which was in good agreement with the above discussion.

Mechanistic studies. Based on the overwhelming evidence from the experimental observations, the pathway of CO₂ reduction to CO over Cu(I)-based catalyst was suggested in Fig. 6a. This process started with the formation of [Cu(H₂O)]⁺, which interacted with CO₂ to generate [Cu(H₂O)(CO₂)]⁺. As aforementioned, H₂CO₃ formed after the reaction of CO₂ and H₂O, thereby the occurrence of transition from [Cu(H₂O)(CO₂)]⁺ to [Cu(H₂CO₃)]⁺, which was similar to the direct CO₂ capture and conversion to fuels over magnesium nanoparticles⁵⁴. Subsequent H⁺/e⁻ transfer reactions^{46,48,70} led to the generation

of [Cu(CO)]⁺, along with the elimination of two H₂O molecules. In the CO₂RR, H⁺ ions originated from the dissociation of H₂O/H₂CO₃ or added acid, and the necessary electrons involved in the reduction of CO₂ to CO were likely from the generated H₂CO₃ (Supplementary Fig. 28 and related discussion). Upon the CO₂ reduction, the O atom in [Cu(H₂O)]⁺ combined with the C atom in CO₂ by the formation of CO, whereas the two O atoms in CO₂ were eliminated by loss of two H₂O molecules. The released H₂O molecules could combine with Cu⁺ to form [Cu(H₂O)]⁺ for the next cycle of CO₂ reduction. Despite this, the oxidation state of copper persisted +1, in good agreement with the previous report⁷⁷.

To gain detailed insight into the reaction mechanism, DFT calculations were carried out to explore the key reaction intermediates and possible reaction pathways. Both the singlet and triplet reaction paths had been considered to understand all possibilities. The singlet reaction path was more thermodynamically favorable than the triplet reaction path, and both paths were similar (Fig. 6b, Supplementary Fig. 29, and Supplementary Table 2–4). Because of this fact, the discussion herein focused mainly on the singlet reaction path with a lower energy.

The activation of CO₂ was initialized with the collision interaction among ¹CO₂, ¹Cu⁺, and ¹H₂O (Supplementary Fig. 30). All calculations on bimolecular interactions indicated that [¹Cu-OH₂]⁺ (¹MS1), through the collision of ¹Cu⁺ and ¹H₂O, was the most preferred possibility in contrast to others, such as ¹Cu⁺ and ¹CO₂ or ¹CO₂ and ¹H₂O. The binding energy of ¹Cu⁺ and ¹H₂O in ¹MS1 was as high as -40.18 kcal mol⁻¹, which was larger than those of ¹Cu⁺ and ¹CO₂ (¹[Cu-O=C=O]⁺, -19.68 kcal mol⁻¹) and ¹CO₂ and ¹H₂O (¹[H₂O-O=C=O]⁺, 2.53 kcal mol⁻¹). In the collision between ¹Cu⁺ and ¹H₂O, ¹Cu⁺ was prone to interact with the central O atom in H₂O to form [¹Cu-OH₂]⁺ through O-Cu coupling with a bond length of 1.90 Å.

The existence of activated $^1[\text{Cu-OH}_2]^+$ ($^1\text{MS1}$) promoted the reduction of $^1\text{CO}_2$. First, $^1\text{CO}_2$ interacted with $^1\text{MS1}$ to form the $^1[\text{Cu-O(H)-H}\cdots\text{OCO}]^+$ ($^1\text{MS2}$, $-40.33 \text{ kcal mol}^{-1}$) intermediate by a weak O-H \cdots O hydrogen bond. The O-C bond length of $^1\text{CO}_2$ changed from 1.16 Å to 1.17 and 1.15 Å in $^1\text{MS2}$. Subsequently, $^1\text{MS2}$ isomerized into $^1[\text{Cu-O(H)-C(O)OH}]^+$ ($^1\text{MS3}$, $-2.84 \text{ kcal mol}^{-1}$) through a transition state, $^1\text{TS2/3}$ ($10.08 \text{ kcal mol}^{-1}$). It is worth noting that in the conversion from $^1\text{TS2/3}$ to $^1\text{MS3}$, the breakage of the O-H bond in H_2O occurred, and the O-H and C-O bonds formed between the H_2O and CO_2 (Supplementary Fig. 31–34). This process was the rate-limiting step of CO_2 reduction with an activation barrier as high as $50.41 \text{ kcal mol}^{-1}$. Further isomerization turned $^1\text{MS3}$ into $^1[\text{Cu-O-C(OH)}_2]^+$ ($^1\text{MS4}$, $-2.84 \text{ kcal mol}^{-1}$), which only involved the migration of intramolecular hydrogen through the transition state $^1\text{TS3/4}$ ($18.74 \text{ kcal mol}^{-1}$), and the activation barrier from $^1\text{MS3}$ to $^1\text{TS3/4}$ was $21.58 \text{ kcal mol}^{-1}$.

Once $^1\text{MS4}$ was generated, two molecules of water were lost by a H^+/e^- transfer process, thereby leading to the formation of $^1[\text{Cu-O-C}]^+$ ($^1\text{MS6}$, $-90.19 \text{ kcal mol}^{-1}$). In the process, H^+/e^- was initially transferred from the reaction system to the OH group of $^1\text{MS4}$, which resulted in the release of one H_2O molecule to form a $^1[\text{Cu-O-COH}]^+$ ($^2\text{MS5}$, $-29.30 \text{ kcal mol}^{-1}$) intermediate. As the OH group in $^2\text{MS5}$ was further attacked by H^+/e^- , a $^1\text{MS6}$ intermediate was formed through the release of another H_2O molecule. The dehydration process would compete with hydrogen evolution reaction (HER). By calculation of their corresponding free energy, the values were $-4.76 \text{ kcal mol}^{-1}$ and $-60.89 \text{ kcal mol}^{-1}$ when $^1\text{MS4}$ and $^2\text{MS5}$ were transferred to $^2\text{MS5}$ and $^1\text{MS6}$, respectively. For a standard hydrogen electrode, the free energy is $-19.09 \text{ kcal mol}^{-1}$ as H^+ is transferred to H_2 in basic solution, which system is favorable to aqueous electrochemical CO_2RR while preventing from HER. Apparently, in contrast to the transfer of $^1\text{MS4}$ to $^2\text{MS5}$, it was prone to the HER, whereas an opposite trend occurred when $^2\text{MS5}$ was transferred to $^1\text{MS6}$. Along with the processes, $^2\text{MS5}$ would also tend to combine with H^+ by formation of $[\text{Cu}(\text{HCOOH})]^+$ as a side reaction, which was captured in our current study (Supplementary Figs. 7a, b and 35).

In the last step, the bound CO group dissociated from $^1\text{MS6}$ by forming an isolated CO molecule and pristine $^1\text{Cu}^+$, thus completing the catalytic cycle and releasing $-82.46 \text{ kcal mol}^{-1}$ of thermal energy. The reaction pathway offers further convincing theoretical evidence for the hypothesized mechanism derived from mass spectrometric analysis. It also details how H_2O molecule is involved in the reduction of CO_2 to CO and how it replaces two O atoms in CO_2 with the one in its structure.

In summary, we have developed a modified TSQ mass spectrometer that enabled online observation of the CO_2RR and detection of the reaction intermediates and products. The results demonstrated that the coordinated H_2O on Cu(I)-based catalysts played a crucial role in the efficiencies of both CO_2 adsorption onto the Cu(I) catalyst and CO_2 reduction to CO, and that an improvement of two orders of magnitude was achieved in the presence of a coordinated H_2O than without H_2O . Further experiments indicated that the existing form of H_2O and the number of coordinated H_2O also had a significant effect on the reduction of CO_2 to CO. More importantly, isotope-labeling investigations revealed that the origin of the O atom in the generated CO originated from H_2O , instead of CO_2 . Based on the experimental observations and computational calculations, the specific pathway for the reduction of CO_2 to CO was proposed. This work not only offers a new strategy to disclose the reaction process of CO_2RR , but also provides useful insight into the roles of H_2O , suggesting the efficiency of CO_2RR could be improved by constructing new types of catalysts with coordinated H_2O .

Methods

Preparation of different Cu-based solutions. Identical procedures were used to prepare the different Cu-based solutions. Specifically, 0.1 g of Cu-based particles such as CuCl were first dissolved into 1.0 mL of double-deionized water. After sonication for 30 min using a KQ3200DB ultrasonic cleaner (Kunshan Ultrasonic Instrument Co., Ltd., Kunshan, China), 1 μL of the CuCl aqueous solution was added into 999 μL of acetonitrile. Finally, the resulting solution was mixed with a QL-901 Vortex oscillator (Haimen Qilin Beier Instrument Manufacturing Co., Ltd., Haimen, China) for 1 min.

Preparation of glass capillary with a tip orifice of 1 μm . A glass capillary with a tip orifice of 1 μm was pulled from borosilicate glass capillary with filament (Sutter Instrument, USA, 1.5 mm o.d., 0.86 mm i.d., 10 cm length) using a micropipette puller (Model P-97, Sutter Instrument Co., Novato, CA, USA). The tip orifice was measured with a metallographic microscope equipped with a DCA 10.0 digital camera (1 million resolution) and had a tip orifice precision of $\pm 1 \mu\text{m}$.

Online reaction and MS analysis. All experiments on nanoelectrospray ionization mass spectrometry (nanoESI-MS) were carried out with either a TSQ Quantum Access Max mass spectrometer or an Orbitrap Elite Hybrid Ion Trap-Orbitrap Mass Spectrometer (Thermo Fisher Scientific, San Jose, CA, USA). For nanoESI, 20 μL of a 100 $\mu\text{g mL}^{-1}$ CuCl solution was injected into a glass capillary with 1 μm of tip orifice, and, subsequently, 1.0 kV of DC voltage was applied to the CuCl solution for the generation of various Cu-based ions. The distance between the nanoESI tip and MS inlet capillary was about 10 mm. Mass spectra were recorded in the positive ion mode with a capillary temperature of 270 °C. The identification of Cu-based ions was confirmed by high-resolution mass spectrometry (HRMS) and tandem mass spectrometry (MS/MS) using collision-induced dissociation (CID). Argon gas (99.995% purity) was used as the collision gas. For the reaction between Cu-based ions and CO_2 , Cu-based ions such as Cu^+ and $[\text{Cu}(\text{H}_2\text{O})]^+$ were first isolated from Q1 and then introduced to Q2 (see Fig. 1). In the reaction unit of Q2, Cu-based ions interacted with CO_2 to yield CO under collision energy of 5 V, and the resulting products were subsequently transferred to Q3, followed by detection. It should be pointed out that the collision energy for CO_2 reduction was controlled by the operation software of employed commercial mass spectrometer. To explore the effect of acid on the reaction of Cu-based ions and CO_2 , 2 μL of acetic acid was injected through a six-way valve (Beijing Yijia Technology Co., Ltd., Beijing, China) into the CO_2/Ar gas circuit system. To enhance the reaction efficiency between Cu-based ions and CO_2 , the gas circuit system was heated to different temperatures via a heating tape controlled by an XMT-815 temperature controller (Shanghai Mike Instrument Co., Ltd., Shanghai, China). The actual temperature of heating tape was determined using a 17B Fluke multimeter (Shanghai Fluke Corporation, Shanghai, China).

Reversed WGS experiment. The experiments were carried out with a WGS apparatus (Tianjin Tongyuan Hengli Technology Co., Ltd, Tianjin, China). The reactor was loaded with 1.0 g of Cu/ZnO/Al $_2$ O $_3$ catalyst. The pressures of H_2^{16}O and H_2^{18}O were controlled by a syringe pump with flow rates ranging from 1 to 50 $\mu\text{L min}^{-1}$. After adjusting a flow rate, a balance time of 1.5 h was used to make the equilibrium of CO_2 reduction reaction. The air and involved contaminants were replaced with H_2 via successive purging. In the reaction process, the reaction partial pressure of H_2 and CO_2 were kept constant at 2.7 MPa and 0.3 MPa, respectively, and the reactor temperature was maintained at 230 °C. The gas products were analyzed online with a Fuli GC9790 gas chromatograph equipped with a TDX-01 molecular sieve packing column (2 m x 3 mm). For the H_2^{18}O -labelling experiments, the collected gas products were analyzed off-line with an Agilent Technologies 7890B gas chromatograph equipped with a GS-CarbonPLOT capillary column (30 m x 0.32 mm I.D., 1.50 μm film thickness) and an Agilent Technologies 5977 A mass spectrometer. The carrier gas was helium with a flow rate of 15 mL min^{-1} . The initial oven temperature was set as 35 °C and maintained for 3 min. Afterward, it was increased to 100 °C with a rate of 40 °C min^{-1} followed by maintaining for 1 min. The injector temperature was 185 °C, and the injection volume was 250 μL with a split ratio of 100:1.

In situ DRIFTS analysis. The in situ diffuse reflectance infrared Fourier transform spectroscopy (in situ DRIFTS) results were conducted on an FTIR (Nicolet 6700) equipped with a Pike DRIFT cell (PIKE Technologies) with a KBr window and an MCT/A detector (cooled by liquid nitrogen). The spectra were collected in the range from 900 to 4000 cm^{-1} with 32 scans, and the resolution was 4 cm^{-1} . All used cylinder gases were of high purity and dried through a moisture trap (Agilent Technologies) before entering the in situ chamber. To minimize the environment interference, the FTIR chamber was purged with argon (99.999%) in a flow rate of 4 L min^{-1} . Prior to the experiment, the sample was treated with hydrogen (99.9999%) in a flow rate of 5 mL min^{-1} for 2 h and then switched to helium (99.9999%) with a flow rate of 5 mL min^{-1} for 2 h at 500 °C to reduce the surface oxide and remove all possible organic contaminants. Subsequently, under the helium flow, the reactor was cooled down to 150 °C or 250 °C for hydrogenation of CO_2 . When a steady baseline was obtained, hydrogen (3 mL min^{-1}) and CO_2

(4 mL min⁻¹, 5% CO₂/95% Ar) were introduced sequentially. To investigate the effect of water on CO₂RR, a syringe needle fulfilled with 1 μL of water was inserted into the tube containing hydrogen flow, enabling the introduction of trace water into the reaction system. The employed catalyst, Cu/γ-Al₂O₃, was prepared by an incipient-wetness impregnation method using the precursors of Cu(NO₃)₂ (>99.0%, Guangzhou Chemical Reagent Factory, Guangzhou, China) and γ-Al₂O₃ powder (99.99%, Energy Chemical Co., Guangzhou, China).

Electrochemical reduction of CO₂ and online mass spectrometer monitoring.

For the electrochemical reduction of CO₂ to CO, the reaction products and CO₂ were monitored with an online differential electrochemical mass spectrometer (DEMS, Linglu Instrument Co., Ltd, Shanghai, China). The configuration of the electrochemical cell is shown in Supplementary Fig. 18. The cell was fulfilled with 2.5 mL of 0.5 M KCl solution, which was saturated with CO₂ gas. During the electrochemical test, a continuous CO₂ gas flow was introduced into KCl solution. The working electrode was prepared by sputtering gold nanoparticles on porous membrane. The reference electrode was an Ag/AgCl electrode in saturated KCl solution, and the counter electrode was Pt wire electrode. The linear sweeping voltammetry was conducted on an electrochemical workstation (CHI Instruments, Inc., Austin, TX, USA) with the sweeping rate of 10 mV s⁻¹ from -0.8 V to -1.6 V. Simultaneously, the MS signals with the mass/charge ratios of 4430, and 28 were recorded by the MS. The ¹⁸O-labeled H₂O (purity: 99.0%, ¹⁸O abundance: ≥98.0%) was purchased from Wuhan Isotope Technology Co., Ltd (Wuhan, China).

Computational details. All electronic structure calculations were performed with the Gaussian 09 package (revision B.01; Gaussian, Inc., Wallingford CT, 2010)⁷⁹. For geometry optimization, we used the B2PLYP double hybrid density functional method⁸⁰ in conjunction with the augmented correlation-consistent polarized triple zeta (aug-cc-pVTZ) basis set with the implicit treatment of scalar-relativistic effects by using the effective core potential (ECP) pseudopotential for the metal atoms⁸¹, and the aug-cc-pVTZ all-electron basis set for all other atoms⁸². Harmonic vibrational frequencies were computed to verify the nature of the stationary points. The minimum structures reported in this work showed only positive eigenvalues of the Hessian matrix, whereas the transition states had one negative eigenvalue. Intrinsic reaction coordinate calculations were also performed to confirm that the transition states were correlated with the designated intermediates^{83–86}. The zero-point vibrational energy (ZPVE) and thermal corrections to the enthalpy were calculated for structures optimized at the B2PLYP/cc-pVTZ level. The thermodynamic functions (ΔH) were estimated within the ideal gas, rigid-rotor, and harmonic oscillator approximations at 298 K and 1 atm. For ease of discussion, the symbols “^SIS” and “^SFS” are used to describe the initial state (IS), intermediate state (MS), and final state (FS), while “^STsm/n” is used for the interconversion transition state between the intermediate states, ^Sm and ^Sn. The left superscript “^S” denotes the spin multiplicity (1 and 3 for singlet and triplet, respectively).

Data availability

Source data are provided with this paper, which can also be available from the corresponding authors on reasonable request.

Received: 22 July 2021; Accepted: 12 April 2022;

Published online: 11 May 2022

References

- Jessop, P. G., Ikariya, T. & Noyori, R. Homogeneous hydrogenation of carbon dioxide. *Chem. Rev.* **95**, 259–272 (1995).
- Qiao, J., Liu, Y., Hong, F. & Zhang, J. A review of catalysts for the electroreduction of carbon dioxide to produce low-carbon fuels. *Chem. Soc. Rev.* **43**, 631–675 (2014).
- Wagner, A., Sahn, C. D. & Reisner, E. Towards molecular understanding of local chemical environment effects in electro- and photocatalytic CO₂ reduction. *Nat. Catal.* **3**, 775–786 (2020).
- Endrődi, B. et al. Operando cathode activation with alkali metal cations for high current density operation of water-fed zero-gap carbon dioxide electrolyzers. *Nat. Energy* **6**, 439–448 (2021).
- Dinh, C.-T. et al. CO₂ electroreduction to ethylene via hydroxide-mediated copper catalysis at an abrupt interface. *Science* **360**, 783–787 (2018).
- Rendón-Calle, A. et al. How symmetry factors cause potential- and facet-dependent pathway shifts during CO₂ reduction to CH₄ on Cu electrodes. *Appl. Catal. B: Environ.* **285**, 119776 (2021).
- Marcandalli, G., Goyal, A. & Koper, M. T. M. Electrolyte effects on the faradaic efficiency of CO₂ reduction to CO on a gold electrode. *ACS Catal.* **11**, 4936–4945 (2021).
- Le, M. et al. Electrochemical reduction of CO₂ to CH₃OH at copper oxide surfaces. *J. Electrochem. Soc.* **158**, E45 (2011).
- Chen, L. et al. Molecular catalysis of the electrochemical and photochemical reduction of CO₂ with earth-abundant metal complexes. Selective production of CO vs HCOOH by switching of the metal center. *J. Am. Chem. Soc.* **137**, 10918–10921 (2015).
- Hou, W. et al. Photocatalytic conversion of CO₂ to hydrocarbon fuels via plasmon-enhanced absorption and metallic interband transitions. *ACS Catal.* **1**, 929–936 (2011).
- Wang, X. et al. Morphology and mechanism of highly selective Cu(II) oxide nanosheet catalysts for carbon dioxide electroreduction. *Nat. Commun.* **12**, 794 (2021).
- Sen, S., Liu, D. & Palmore, G. T. R. Electrochemical reduction of CO₂ at copper nanofoams. *ACS Catal.* **4**, 3091–3095 (2014).
- Lee, S., Park, G. & Lee, J. Importance of Ag–Cu biphasic boundaries for selective electrochemical reduction of CO₂ to ethanol. *ACS Catal.* **7**, 8594–8604 (2017).
- Rudolph, M., Dautz, S. & Jäger, E.-G. Macrocyclic [N₄²⁻] coordinated nickel complexes as catalysts for the formation of oxalate by electrochemical reduction of carbon dioxide. *J. Am. Chem. Soc.* **122**, 10821–10830 (2000).
- Chang, X., Wang, T. & Gong, J. CO₂ photo-reduction: insights into CO₂ activation and reaction on surfaces of photocatalysts. *Energ. Environ. Sci.* **9**, 2177–2196 (2016).
- Choi, K. M. et al. Plasmon-enhanced photocatalytic CO₂ conversion within metal–organic frameworks under visible light. *J. Am. Chem. Soc.* **139**, 356–362 (2017).
- Robatjazi, H. et al. Plasmon-induced selective carbon dioxide conversion on earth-abundant aluminum-cuprous oxide antenna-reactor nanoparticles. *Nat. Commun.* **8**, 27 (2017).
- Tan, X. et al. Recent advances in innovative strategies for the CO₂ electroreduction reaction. *Energ. Environ. Sci.* **14**, 765–780 (2021).
- Guo, W. et al. Atomic indium catalysts for switching CO₂ electroreduction products from formate to CO. *J. Am. Chem. Soc.* **143**, 6877–6885 (2021).
- Jiang, X., Nie, X., Guo, X., Song, C. & Chen, J. G. Recent advances in carbon dioxide hydrogenation to methanol via heterogeneous catalysis. *Chem. Rev.* **120**, 7984–8034 (2020).
- Deng, Y. & Yeo, B. S. Characterization of electrocatalytic water splitting and CO₂ reduction reactions using in situ/operando Raman spectroscopy. *ACS Catal.* **7**, 7873–7889 (2017).
- Lin, S.-C. et al. Operando time-resolved X-ray absorption spectroscopy reveals the chemical nature enabling highly selective CO₂ reduction. *Nat. Commun.* **11**, 3525 (2020).
- Nguyen, L., Tao, F. F., Tang, Y., Dou, J. & Bao, X.-J. Understanding catalyst surfaces during catalysis through near ambient pressure X-ray photoelectron spectroscopy. *Chem. Rev.* **119**, 6822–6905 (2019).
- Zou, Y. & Wang, S. An investigation of active sites for electrochemical CO₂ reduction reactions: From in situ characterization to rational design. *Adv. Sci.* **8**, 2003579 (2021).
- Bendavid, L. I. & Carter, E. A. CO₂ adsorption on Cu₂O(111): A DFT+U and DFT-D study. *J. Phys. Chem. C* **117**, 26048–26059 (2013).
- Mishra, A. K. & de Leeuw, N. H. Mechanistic insights into the Cu(I) oxide-catalyzed conversion of CO₂ to fuels and chemicals: A DFT approach. *J. CO₂ Util.* **15**, 96–106 (2016).
- Wang, X. et al. Elucidating the reaction mechanisms between triazine and hydrogen sulfide with pH variation using mass spectrometry. *Anal. Chem.* **90**, 11138–11145 (2018).
- Banerjee, S., Basheer, C. & Zare, R. N. A study of heterogeneous catalysis by nanoparticle-embedded paper-spray ionization mass spectrometry. *Angew. Chem. Int. Ed.* **55**, 12807–12811 (2016).
- Li, Y., Yan, X. & Cooks, R. G. The Role of the interface in thin film and droplet accelerated reactions studied by competitive substituent effects. *Angew. Chem. Int. Ed.* **55**, 3433–3437 (2016).
- Frick, E., Anastasaki, A., Haddleton, D. M. & Barner-Kowollik, C. Enlightening the mechanism of copper mediated photoRDRP via high-resolution mass spectrometry. *J. Am. Chem. Soc.* **137**, 6889–6896 (2015).
- Gu, C. et al. Mechanistic study of oxygen reduction at liquid/liquid interfaces by hybrid ultramicroelectrodes and mass spectrometry. *J. Am. Chem. Soc.* **141**, 13212–13221 (2019).
- Clark, E. L. & Bell, A. T. Direct observation of the local reaction environment during the electrochemical reduction of CO₂. *J. Am. Chem. Soc.* **140**, 7012–7020 (2018).
- Wilm, M. & Mann, M. Analytical properties of the nano-electrospray ion source. *Anal. Chem.* **68**, 1–8 (1996).
- Guzmán, H., Russo, N. & Hernández, S. CO₂ valorisation towards alcohols by Cu-based electrocatalysts: challenges and perspectives. *Green. Chem.* **23**, 1896–1920 (2021).
- Gawande, M. B. et al. Cu and Cu-based nanoparticles: synthesis and applications in catalysis. *Chem. Rev.* **116**, 3722–3811 (2016).

36. Yoshio, H., Katsube, K. & Shin, S. Production of CO and CH₄ in electrochemical reduction of CO₂ at metal electrodes in aqueous hydrogencarbonate solution. *Chem. Lett.* **14**, 1695–1698 (1985).
37. Zhu, C. et al. Product-specific active site motifs of Cu for electrochemical CO₂ reduction. *Chem* **7**, 406–420 (2021).
38. Wang, Y. et al. Catalyst synthesis under CO₂ electroreduction favours faceting and promotes renewable fuels electrosynthesis. *Nat. Catal.* **3**, 98–106 (2020).
39. Zhou, Y. et al. Dopant-induced electron localization drives CO₂ reduction to C₂ hydrocarbons. *Nat. Chem.* **10**, 974–980 (2018).
40. Zhao, Q., Martinez, J. M. P. & Carter, E. A. Revisiting understanding of electrochemical CO₂ reduction on Cu(111): competing proton-coupled electron transfer reaction mechanisms revealed by embedded correlated wavefunction theory. *J. Am. Chem. Soc.* **143**, 6152–6164 (2021).
41. Li, X., Wang, S., Li, L., Sun, Y. & Xie, Y. Progress and perspective for in situ studies of CO₂ reduction. *J. Am. Chem. Soc.* **142**, 9567–9581 (2020).
42. Wang, W.-N. et al. Size and structure matter: enhanced CO₂ photoreduction efficiency by size-resolved ultrafine Pt nanoparticles on TiO₂ single crystals. *J. Am. Chem. Soc.* **134**, 11276–11281 (2012).
43. Li, J. et al. Interfacial engineering of Bi₁₉Br₃S₂₇ nanowires promotes metallic photocatalytic CO₂ reduction activity under near-infrared light irradiation. *J. Am. Chem. Soc.* **143**, 6551–6559 (2021).
44. Ra, E. C. et al. Recycling carbon dioxide through catalytic hydrogenation: recent key developments and perspectives. *ACS Catal.* **10**, 11318–11345 (2020).
45. Leung, K., Nielsen, I. M. B., Sai, N., Medforth, C. & Shelnutt, J. A. Cobalt –porphyrin catalyzed electrochemical reduction of carbon dioxide in water. *2. Mechanism first Princ. J. Phys. Chem. A* **114**, 10174–10184 (2010).
46. Wang, X. et al. Proton capture strategy for enhancing electrochemical CO₂ reduction on atomically dispersed metal–nitrogen active sites. *Angew. Chem. Int. Ed.* **133**, 12066–12072 (2021).
47. Burkart, M. D., Hazari, N., Tway, C. L. & Zeitler, E. L. Opportunities and challenges for catalysis in carbon dioxide utilization. *ACS Catal.* **9**, 7937–7956 (2019).
48. Bonetto, R., Crisanti, F. & Sartorel, A. Carbon dioxide reduction mediated by iron catalysts: mechanism and intermediates that guide selectivity. *ACS Omega* **5**, 21309–21319 (2020).
49. Zhu, H.-J. et al. Efficient electron transmission in covalent organic framework nanosheets for highly active electrocatalytic carbon dioxide reduction. *Nat. Commun.* **11**, 497 (2020).
50. Francke, R., Schille, B. & Roemelt, M. Homogeneously catalyzed electroreduction of carbon dioxide—methods, mechanisms, and catalysts. *Chem. Rev.* **118**, 4631–4701 (2018).
51. Wei, Q. et al. Recognition of water-induced effects toward enhanced interaction between catalyst and reactant in alcohol oxidation. *J. Am. Chem. Soc.* **143**, 6071–6078 (2021).
52. Koishybay, A. & Shantz, D. F. Water Is the oxygen source for methanol produced in partial oxidation of methane in a flow reactor over Cu-SSZ-13. *J. Am. Chem. Soc.* **142**, 11962–11966 (2020).
53. Liu, Z. et al. Water-promoted interfacial pathways in methane oxidation to methanol on a CeO₂/Cu₂O catalyst. *Science* **368**, 513–517 (2020).
54. Rawool, S. A. et al. Direct CO₂ capture and conversion to fuels on magnesium nanoparticles under ambient conditions simply using water. *Chem. Sci.* **12**, 5774–5786 (2021).
55. Yang, P.-P. et al. Protecting copper oxidation state via intermediate confinement for selective CO₂ electroreduction to C₂₊ fuels. *J. Am. Chem. Soc.* **142**, 6400–6408 (2020).
56. Wang, W. et al. Photocatalytic C–C coupling from carbon dioxide reduction on copper oxide with mixed-valence copper(I)/copper(II). *J. Am. Chem. Soc.* **143**, 2984–2993 (2021).
57. Chou, T.-C. et al. Controlling the oxidation state of the Cu electrode and reaction intermediates for electrochemical CO₂ reduction to ethylene. *J. Am. Chem. Soc.* **142**, 2857–2867 (2020).
58. Wu, Z.-Z., Gao, F.-Y. & Gao, M.-R. Regulating the oxidation state of nanomaterials for electrocatalytic CO₂ reduction. *Energ. Environ. Sci.* **14**, 1121–1139 (2021).
59. Kreft, S. et al. Improving selectivity and activity of CO₂ reduction photocatalysts with oxygen. *Chem* **5**, 1818–1833 (2019).
60. He, Q. et al. Rapid screening of copper intermediates in Cu(I)-catalyzed azide–alkyne cycloaddition using a modified ICP-MS/MS platform. *Chem. Commun.* **52**, 10501–10504 (2016).
61. He, Q. et al. Rapid screening of gaseous catalysts in methane activation using ICP-QQ-MS. *J. Anal. At. Spectrom.* **33**, 563–568 (2018).
62. Souda, R., Kawanowa, H., Kondo, M. & Gotoh, Y. Hydrogen bonding between water and methanol studied by temperature-programmed time-of-flight secondary ion mass spectrometry. *J. Chem. Phys.* **119**, 6194–6200 (2003).
63. Vöhringer-Martinez, E. et al. Hydrogen bond dynamics of superheated water and methanol by ultrafast IR-pump and EUV-photoelectron probe spectroscopy. *Phys. Chem. Chem. Phys.* **16**, 19365–19375 (2014).
64. Hantal, G., Terlezky, P., Horvai, G., Nyulászi, L. & Jedlovsky, P. Molecular level properties of the water–dichloromethane liquid/liquid interface, as seen from molecular dynamics simulation and identification of truly interfacial molecules analysis. *J. Phys. Chem. C* **113**, 19263–19276 (2009).
65. Gopi, R., Ramanathan, N. & Sundararajan, K. Acetonitrile–water hydrogen-bonded interaction: Matrix-isolation infrared and ab initio computation. *J. Mol. Struct.* **1094**, 118–129 (2015).
66. Finneran, I. A., Carroll, P. B., Allodi, M. A. & Blake, G. A. Hydrogen bonding in the ethanol–water dimer. *Phys. Chem. Chem. Phys.* **17**, 24210–24214 (2015).
67. Dawes, A. et al. Probing the interaction between solid benzene and water using vacuum ultraviolet and infrared spectroscopy. *Phys. Chem. Chem. Phys.* **20**, 15273–15287 (2018).
68. Michoulier, E. et al. Perturbation of the surface of amorphous solid water by the adsorption of polycyclic aromatic hydrocarbons. *J. Phys. Chem. C* **124**, 2994–3001 (2020).
69. Queiroz, M. H., Alves, T. V. & Rivelino, R. A theoretical screening of the OH...π interaction between water and benzene using density-functional approaches: Effects of nonlocal exchange and long-range dispersion corrections in the true minimum. *Comput. Theor. Chem.* **1206**, 113464 (2021).
70. Yuan, X. et al. Ultrathin Pd–Au shells with controllable alloying degree on pd nanocubes toward carbon dioxide reduction. *J. Am. Chem. Soc.* **141**, 4791–4794 (2019).
71. Sasaki, M., Tachibana, Y. & Fujinaka, Y. Catalytic activity of the H₂O/CO₂ system in lignocellulosic-material decomposition. *Ind. Eng. Chem. Res.* **58**, 9239–9245 (2019).
72. Stirling, A. & Pápai, I. H₂CO₃ forms via HCO₃[−] in water. *J. Phys. Chem. B* **114**, 16854–16859 (2010).
73. Tossell, J. A. H₂CO₃(s): A new candidate for CO₂ capture and sequestration. *Environ. Sci. Technol.* **43**, 2575–2580 (2009).
74. Zhao, J. et al. An overview of Cu-based heterogeneous electrocatalysts for CO₂ reduction. *J. Mater. Chem. A* **8**, 4700–4734 (2020).
75. Velasco-Vélez, J.-J. et al. The role of the copper oxidation state in the electrocatalytic reduction of CO₂ into valuable hydrocarbons. *ACS Sustain. Chem. Eng.* **7**, 1485–1492 (2019).
76. Liang, Z.-Q. et al. Copper-on-nitride enhances the stable electrosynthesis of multi-carbon products from CO₂. *Nat. Commun.* **9**, 3828 (2018).
77. Mistry, H. et al. Highly selective plasma-activated copper catalysts for carbon dioxide reduction to ethylene. *Nat. Commun.* **7**, 12123 (2016).
78. De Luna, P. et al. Catalyst electro-redeposition controls morphology and oxidation state for selective carbon dioxide reduction. *Nat. Catal.* **1**, 103–110 (2018).
79. Frisch, M. J. et al. Gaussian 09 Rev. B.01 (Gaussian, Inc., Wallingford, CT, USA, 2010).
80. Grimme, S. Semiempirical hybrid density functional with perturbative second-order correlation. *J. Chem. Phys.* **124**, 034108 (2006).
81. Peterson, K. A. & Puzzarini, C. Systematically convergent basis sets for transition metals. II. Pseudopotential-based correlation consistent basis sets for the group 11 (Cu, Ag, Au) and 12 (Zn, Cd, Hg) elements. *Theor. Chem. Acc.* **114**, 283–296 (2005).
82. Dunning, T. H. Jr. Gaussian basis sets for use in correlated molecular calculations. I. The atoms boron through neon and hydrogen. *J. Chem. Phys.* **90**, 1007–1023 (1989).
83. Truhlar, D. G. & Gordon, M. S. From force fields to dynamics: classical and quantal paths. *Science* **249**, 491–498 (1990).
84. Gonzalez, C. & Schlegel, H. B. Reaction path following in mass-weighted internal coordinates. *J. Phys. Chem.* **94**, 5523–5527 (1990).
85. Fukui, K. The path of chemical reactions - the IRC approach. *Acc. Chem. Res.* **14**, 363–368 (1981).
86. Fukui, K. Formulation of the reaction coordinate. *J. Phys. Chem.* **74**, 4161–4163 (1970).

Acknowledgements

The authors thank Professor R. Zare at Stanford University, Professor D. Li at China Three Gorges University, and Prof. Y. Lan at Nanjing Normal University for valuable suggestions and Dr. L. Ding at Xi'an Shiyou University for performing the reversed water-gas shift reaction experiments. Z.Z. thanks the National Natural Science Foundation of China for Project 21777128, the Natural Science Basic Research Program of Shaanxi Province of China for Project 2019JC-33, and the Youth Innovation Team of Shaanxi Universities for Project Z19257. Y.Z. thanks the Natural Science Basic Research Program of Shaanxi Province of China for Project 2021GY-247.

Author contributions

Z.Z., Y.Z., Q.W., and G.Y. devised the initial concept for the work, Z.Z. and Y.Z. designed the experiments, H.Y., R.D., Z.X., F.L., G.Y., and Y.L. carried out the experiments and

analyzed the data. Z.Z., Q.W., Y.Z., G.Y., and Q.M. co-wrote the manuscript. All authors discussed the results and commented on the manuscript at all stages.

Competing interests

The authors declare no competing interests.

Additional information

Supplementary information The online version contains supplementary material available at <https://doi.org/10.1038/s41467-022-30289-5>.

Correspondence and requests for materials should be addressed to Qiang Wang, Guangxing Yang or Zhiping Zhang.

Peer review information *Nature Communications* thanks Kazuhiro Takanabe, Alimohammad Bahmanpour and the other, anonymous, reviewer for their contribution to the peer review of this work. Peer reviewer reports are available.

Reprints and permission information is available at <http://www.nature.com/reprints>

Publisher's note Springer Nature remains neutral with regard to jurisdictional claims in published maps and institutional affiliations.



Open Access This article is licensed under a Creative Commons Attribution 4.0 International License, which permits use, sharing, adaptation, distribution and reproduction in any medium or format, as long as you give appropriate credit to the original author(s) and the source, provide a link to the Creative Commons license, and indicate if changes were made. The images or other third party material in this article are included in the article's Creative Commons license, unless indicated otherwise in a credit line to the material. If material is not included in the article's Creative Commons license and your intended use is not permitted by statutory regulation or exceeds the permitted use, you will need to obtain permission directly from the copyright holder. To view a copy of this license, visit <http://creativecommons.org/licenses/by/4.0/>.

© The Author(s) 2022